CHAPTER 6

DNA TRANSLESION SYNTHESIS SUPPRESSES AGING AND AGING-ASSOCIATED CANCER

Anastasia Tsaalbi-Shtylik, Piya Temviriyanukul, Ronald P. van Os, Lieneke M. Uittenboogaard, Keiji Hashimoto, Marinus R. Heideman, Bertien Dethmers-Ausema, Johan W.A. Verspuy, Raoul V. Kuiper, Daniela C.F. Salvatori, Willy M. Baarends, Heinz Jacobs, Masaaki Moriya, Gerald de Haan, Jan H.J. Hoeijmakers and Niels de Wind

Manuscript in preparation

ABSTRACT

The attrition of stem cells and of proliferating compartments that characterizes aging correlates with the accumulation of endogenous DNA lesions during life. To explore the existence of a causal relation between replicative stress at unrepaired endogenous DNA lesions and aging we used mice deficient for the translesion replication gene *Rev1*. *Rev1*$^{-/-}$ mice displayed stem cell attrition and mild progeroid phenotypes that were exacerbated by simultaneous deficiency of the global-genome nucleotide excision repair (GG-NER) gene *Xpc*. *Rev1*$^{-/-}$*Xpc*$^{-/-}$ mice displayed chronic replicative stress, cellular senescence and apoptosis in proliferating compartments, and predisposition to aging-associated lymphomas. We demonstrate the involvement of Rev1 in replicative bypass of peroxidated lipid aldehyde-DNA adducts, a known aging marker and GG-NER substrate. Replicative stress did not induce compensatory somatotrophic suppression, unlike transcriptional stress. Combined, these data provide strong support for a causal role in aging of replicative stress at accumulating endogenous bulky DNA adducts.

Aging is associated with the accumulation of endogenous DNA lesions, with the attrition of stem cells and with the loss of proliferative compartments (Chou *et al.*, 2010; Dykstra *et al.*, 2011; Geiger *et al.*, 2009; Hoeijmakers, 2009; Maslov *et al.*, 2009; Rossi *et al.*, 2007; Ruzankina *et al.*, 2008; Wang *et al.*, 2012; Winczura *et al.*, 2012). However, the mechanistic relation between DNA damage and aging largely is elusive. Most damaged genomic nucleotides are repaired by excision repair pathways, including GG-NER that specifically repairs bulky and helix-distorting nucleotide lesions (Hoeijmakers, 2009). During DNA replication, damaged nucleotides that have evaded repair require specialized bypass mechanisms that thereby suppress replicative stress and genome instability. Translesion replication (TLR) comprises a set of specialized DNA polymerases with reduced template stringency and is a major pathway to replicate damaged nucleotides (Sale *et al.*, 2012). Since *Rev1* is a key regulator of TLR (Jansen *et al.*, 2006; Sale *et al.*, 2012), we argued that *Rev1*-deficient (*Rev1*) mice would be useful tools to investigate the involvement of replicative stress at unrepaired endogenous DNA lesions in aging.

Rev1 embryos were present at the expected ratio and displayed no overt defects (Figs. S2A and B). *Rev1* pups were slightly underrepresented and the mice displayed mild growth retardation (Figs. S2A-D), supporting previous data (Jansen *et al.*, 2006). Moreover, the median and maximal lifespans of *Rev1* mice were reduced, and they prematurely developed an aged appearance (Figs. S2E and F). Compared with age-matched wild type littermates, livers of these *Rev1* mice displayed enhanced signs of aging-associated degeneration, including steatosis, karyomegaly, and accumulation of the lipid degradation product lipofuscin (Thoolen *et al.*, 2010) (Figs. S3A and B; Table S1). In all *Rev1* mice gonads were unusually small (Fig. 1A). Ovaries were depleted of follicles and in most testicular tubules spermatogenesis was absent (Figs. S3C and D). Gonads were largely devoid of cells positive for the germ cell marker GCNA1 already in juvenile *Rev1* mice (Wang *et al.*, 1996) (Figs. 1B, Figs. S3E and F), indicating an early germ cell defect. In adult *Rev1* mice, GCNA1 staining appeared normal in the residual follicles and active seminiferous tubules, and these displayed normal spermatogenesis (Figs. S3D and G). Indeed, *Rev1* males occasionally begot progeny.

In most aged *Rev1* mice the cellularity of the bone marrow was reduced, compared with the controls (Fig. 1C and Table S1). To further analyse the hematopoietic compartment of the *Rev1* mice, we isolated quiescent hematopoietic stem cells (HSCs; LSK $CD48^-$ $CD34^-$ $EPCR^+$ $CD150^+$) and derived hematopoietic progenitors (LSK and LSK $CD34^-$) (Dykstra *et al.*, 2011) from bone marrow of 18-months old mice, prior to the onset of aging pathology. The absolute and relative frequencies of these cell types did not significantly differ between the genotypes (Fig. 1D). *Rev1* HSCs displayed wild type viability upon mitogenic stimulation *in vitro*, as assessed with a cobblestone area forming colony (CAFC) assay (Fig. 1E). However, when grown in cytokine-supplemented cultures, the size of the *Rev1* colonies was reduced, compared with controls, indicating a proliferative defect ($p<0.001$, Fig. S4). To investigate the *in*

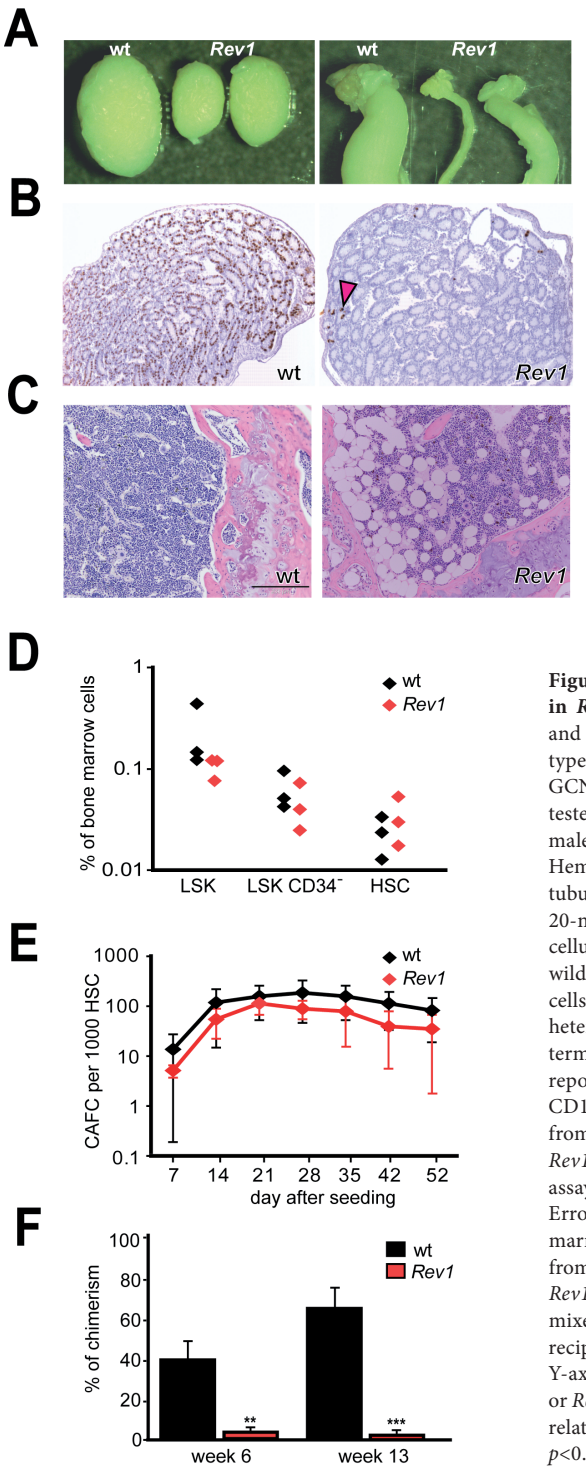

Figure 1 | Germ and stem cell attrition in *Rev1* mice. (A) Bouin-fixed testes (left) and ovaries (right) of 2 month-old wild type and Rev1 littermates. **(B)** Staining for GCNA1-positive (brown) germ cells in testes from 6 day-old wild type and *Rev1* males. Sections were counterstained with Hematoxylin. Arrowhead: GCNA1-positive tubules. **(C)** Section of the femur of a 20-month old *Rev1* mouse revealing loss of cellularity compared with an age-matched wild type control. Dark blue: hematopoietic cells. Size bar: 200 µM. **(D)** Frequencies of heterogeneous Lin$^-$Sca-1$^+$c-kit$^+$ (LSK), short-term repopulating LSK CD34$^-$ and long-term repopulating HSC (LSK CD48$^-$ CD34$^-$ EPCR$^+$ CD150$^+$) cells, isolated from bone marrow from healthy 18 month-old wild type and *Rev1* mice. **(E)** *In vitro* proliferation (CAFC) assay of HSCs isolated from bone marrow. Error bars: SD. **(F)** Competitive *in vivo* bone marrow repopulation assay of HSCs isolated from bone marrow from 3 wild type and *Rev1* donors. For each donor, 200 HSCs were mixed with 1.2x10^6 W41.SJl competitors per recipient (3-5 recipients per experiment). The Y-axis depicts the contribution of wild type or *Rev1* cells to the repopulated bone marrow, relative to the competitors. **: p<0.01, ***: p<0.001, two-tailed t-test. Error bars: SD.

vivo functionality of the HSCs, we measured their capacity to reconstitute the bone marrow of lethally irradiated recipients using a competitive repopulation assay. This experiment revealed a highly significant competitive defect of the *Rev1* HSCs (Fig. 1F). A decline in the competitive repopulation capacity of HSCs is characteristic also of physiological aging (Dykstra *et al.*, 2011; Geiger *et al.*, 2009).

The failure of *Rev1* germ cells and HSCs to (re)populate their respective compartments, and the progeroid phenotypes of *Rev1* mice, suggested a causal relation between replicative stress at endogenous DNA lesions, the attrition of proliferating cells, and aging. Rev1-mediated TLR is required for the replicative bypass of nucleotide lesions that have escaped repair by GG-NER, as was illustrated by the synergistic hypersensitivity to ultraviolet light of *Rev1Xpc* mice and mouse embryonic fibroblasts (MEFs; Fig. S5). We reasoned that exacerbation of the *Rev1* aging phenotypes by simultaneous GG-NER deficiency would provide evidence of a causal role for bulky nucleotide adducts. To test this, we analyzed cohorts of *Rev1Xpc* double and *Xpc* single-deficient mice. *Xpc* mice develop lung tumors at advanced age, but otherwise do not display spontaneous phenotypes (Melis *et al.*, 2008). *Rev1Xpc* embryos were present at the expected frequency but displayed stochastic abnormalities (Figs. 2A and B). *Rev1Xpc* pups were strongly underrepresented (Fig. 2A). Juvenile *Rev1Xpc* mice displayed no overt abnormalities, besides variably reduced sizes (Fig. 2C and Fig. S5C). However, at different age and with variable severity, degenerative phenotypes became apparent, including cachexia, anemia, and kyphosis (Fig. 2D), and the average and maximal lifespans of the *Rev1Xpc* mice were significantly reduced (Fig. 2E). Eight of these progeroid *Rev1Xpc* mice were sacrificed when moribund (6-13 months old; Fig. 2E and Supplementary Table 1), and analysed for features of aging. Livers of most *Rev1Xpc* mice displayed high levels of steatosis, karyomegaly and accumulated lipofuscin (Figs. 2F-H). Also in kidneys karyomegaly was observed (Figs. S6A and B). The gonads of *Rev1Xpc* mice mimicked those of the *Rev1* mice. The epidermis of all tested *Rev1Xpc* mice was atrophic and keratotic, displaying a reduced number of cell layers (Fig. 2I) suggesting decay of the proliferating basal layer, whereas subcutaneous fat was lacking (Fig. S6C). Most significantly, the bone marrow of *Rev1Xpc* mice was virtually devoid of hematopoietic cells, suggestive of aplastic anemia (Fig. 2J).

The attenuation of lymphoid lineages is a characteristic of aging mice (Dykstra *et al.*, 2011; Geiger *et al.*, 2009). To investigate the lymphoid compartment in spleens from *Rev1Xpc* mice, we quantified B and T lymphocytes using bivariate fluorescent cytometry. In young *Rev1Xpc* mice, T and B cell compartments were normal (Figs. S7G and S8G). In contrast, in spleens of aging *Rev1Xpc* mice the naïve, IgM^+IgD^+, B-cell population was strongly reduced, compared with age-matched *Xpc* controls (Figs. 3A and B; Fig. S7). Whereas the $CD4^+$ (helper) T cell population appeared normal, the $CD8^+$ (cytotoxic) T cell population was attenuated in some of the *Rev1Xpc* spleens (Fig. 3C and Fig. S8). Strikingly, in a significant fraction of the *Rev1Xpc* mice (X^2, p=0.03), spleens and/or lymph nodes were enlarged (Fig. S8M). Analysis

A

Rev1$^{+/-}$ *Xpc*$^{-/-}$ X *Rev1*$^{+/-}$ *Xpc*$^{-/-}$	Number of progeny genotyped	*Rev1Xpc* progeny		
		observed	expected	observed/ expected
13.5-day embryos	67	18 (27%)	17 (25%)	1.1 (p=0.85)
10-day pups	254	7 (2.8%)	64 (25%)	0.1 (p<0.001)

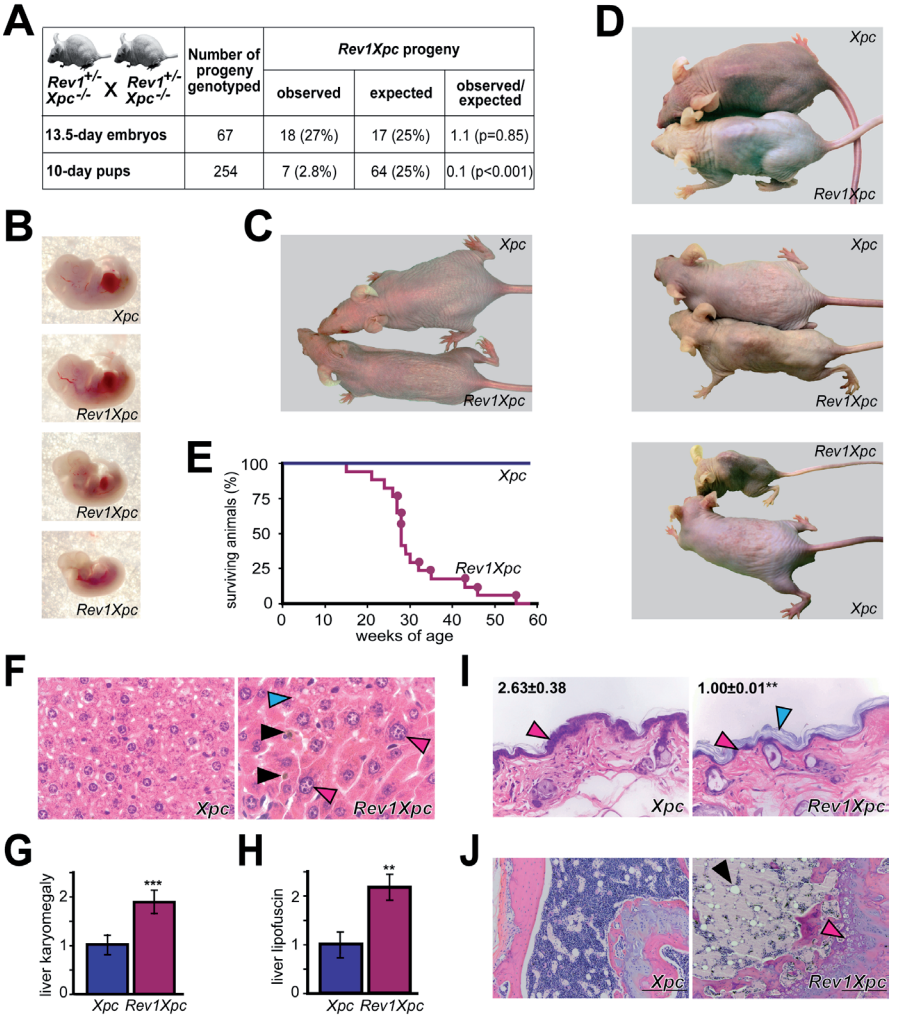

Figure 2 | Progressively degenerative phenotypes of *Rev1Xpc* embryos and mice. **(A)** Frequencies of live 13.5-day *Rev1Xpc* embryos and pups from *Rev1*$^{+/-}$*Xpc*$^{-/-}$ backcrosses. **(B)** Stochastic aberrations of 13.5-day *Rev1Xpc* embryos. Note developmental defects in forebrain and hindbrain, and defective vascularization, of the two bottom *Rev1Xpc* embryos, whereas the embryonic liver is absent in the bottom embryo. **(C)** A 2 months old *Rev1Xpc* mouse displaying a reduced body size, but no other overt phenotypes. **(D)** Overt stochastic features of progeroid *Rev1Xpc* mice include kyphosis, cachexia and anemia. Top and bottom pairs are littermates of 5 months old. The middle pair is the same as shown in Fig. 1C, but here at the age of 12 months. **(E)** Kaplan-Meier survival curve of the cohorts of *Rev1Xpc* mice and *Xpc* littermates (n=17 per cohort). Significantly reduced lifespan (t_{50}=28 weeks; Mann-Whitney test, p<0.001). Spheres refer to mice subjected to extensive autopsy (Table S1). **(F)** Hematoxylin-Eosin (HE) staining of liver sections of 8-month old mice. Blue arrowhead: steatosis. Purple arrowheads: karyomegaly (indicative of polyploidization), black arrowheads: lipofuscin inclusions. **(G)** Relative levels of hepatic karyomegaly. ***: p<0.001. Error bars: SD. **(H)** Relative levels of hepatic lipofuscin. **: p<0.01. Error bars: SD. **(I)** HE staining of skin sections. The numbers refer to the number of epidermal cell layers (±SD, **: p<0.01; purple arrowheads). Blue arrowhead: keratosis of the *Rev1Xpc* epidermis. Also see Fig. S6C. **(J)** HE staining of a section from femurs. Black arrowhead: loss of bone marrow (aplastic anaemia) in the *Rev1Xpc* mouse. Purple arrowhead: bone resorption, indicating osteoporosis. Size bars: 200 μM.

of these spleens revealed the presence of disseminated $CD4^+CD8^+$ (immature T cell) lymphomas (Fig. 3D; Figs. S8J and K), a malignancy common to physiologically aging mice (Frith *et al.*, 1981). In contrast to these proliferating tissues, in (non-proliferating) brains of *Rev1Xpc* mice, no macroscopic or microscopic alterations were found, which differs from mice deficient for the transcription-coupled NER subpathway, in which transcriptional stress causes segmental progeria (Hoeijmakers, 2009; Niedernhofer *et al.*, 2006).

Based on the synergy between the *Rev1* and *Xpc* defects in embryonic, aging and cancer phenotypes we predicted that replicative stress at unrepaired endogenous DNA lesions is increased in the *Rev1Xpc* mice. Indeed, splenocytes from progeroid *Rev1Xpc* mice displayed increased, but variable, levels of phosphorylated H2AX (γH2AX), a marker of replicative stress and associated double-strand DNA breaks that characterizes senescent cells in aging mice (Wang *et al.*, 2009) (Fig. 3E). Consistently, expression of the senescence and aging-related genes $p16^{Ink4A}$ (Ruzankina *et al.*, 2008; Geiger *et al.*, 2009) and *Gadd45A* (Passos *et al.,* 2010) was increased (Fig. 3F) and abundant apoptosis was observed in the *Rev1Xpc* spleens (Figs. 3G and H). We conclude that replicative stress at endogenous DNA lesions induces senescence and apoptosis of proliferating cells in *Rev1Xpc* mice.

We then investigated the nature of the endogenous bulky DNA lesions responsible for the progeroid phenotypes of *Rev1* and, more prominent, *Rev1Xpc* mice. The aging-related phenotypes of the skin (Chen *et al.*, 2012), liver (Gorla *et al.*, 2001; Thoolen *et al.*, 2010), germ cells (Turner *et al.*, 2008), HSCs (Yahata *et al.*, 2011) and lymphoid cells (Geiger *et al.*, 2009) have all been associated with oxidative stress. We therefore focused on bulky DNA lesions that can be induced by oxidative stress. Two such lesions prevail: cyclopurines and lipid peroxide-induced hydroxyalkenal (aldehyde)-DNA adducts (Wang *et al.*, 2012; Winczura *et al.*, 2012). HSCs express high levels of detoxifying aldehyde dehydrogenases (Storms *et al.*, 2005), and acetaldehyde can induce aplastic anemia, resembling the spontaneous aplasia of the *Rev1* and *Rev1Xpc* bone marrow (Langevin *et al.*, 2011). *Rev1* and *Rev1Xpc* cells are not sensitive to acetaldehyde (Langevin *et al.*, 2011). Therefore we hypothesized that, rather than simple aldehyde-DNA adducts, hydroxyalkenal-DNA adducts may underlie the phenotypes of *Rev1* and *Rev1Xpc* mice. In support, compared with *Xpc* MEFs, *Rev1Xpc* MEFs were hypersensitive to the oxidative agent Paraquat and to the lipid peroxide 4-hydroxynonenal (HNE; Fig. 4A). We directly investigated a role of Rev1 in TLR of Heptanone etheno-2-deoxycytidine (H-εdC), a very common hydroxyalkenal-nucleotide adduct that is derived from endogenous, HNE-related, 4-oxononenal (Winczura *et al.*, 2012). This was done by transfection of a plasmid vector containing a site-specific H-εdC into *Rev1* and wild type MEFs (Fig. 4B). In *Rev1* MEFs, the TLR efficiency dropped to 27% of wild type, and the frequency of the incorporation of adenine at the lesion was reduced (X^2 test, $p<0.001$; Fig. 4B).

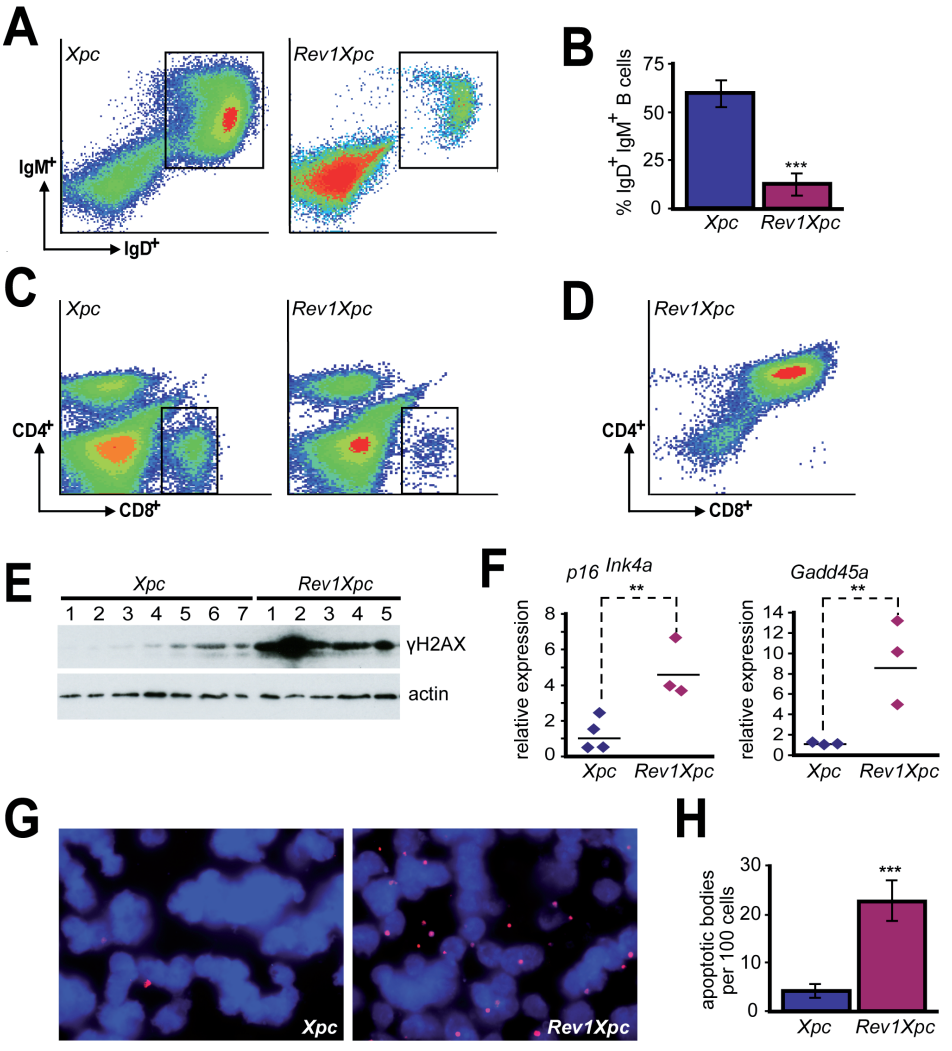

Figure 3 | Decay of lymphocyte populations, increased DNA damage signaling, senescence and apoptosis in spleens from progeroid *Rev1Xpc* mice. **(A)** Fluorescent cytometry of IgM^+IgD^+ B lymphocytes (boxed) from the spleen of a *Rev1Xpc* mouse and an age-matched *Xpc* control. **(B)** Quantification of IgM^+IgD^+ B-cells in spleens from 5 *Rev1Xpc* mice and 6 *Xpc* controls. See Fig. S5. ***: $p<0.001$. Error bars: SD. **(C)** Fluorescent cytometry of $CD4^+$ and $CD8^+$ T lymphocyte populations in spleens of a progeroid *Rev1Xpc* mouse and an age-matched *Xpc* control mouse. See Fig. S6 for examples of stochasticity. **(D)** $CD4^+CD8^+$ T-cell lymphoma in the spleen of a 6 month-old *Rev1Xpc* mouse. **(E)** Western blot displaying γH2AX levels in spleens from 5 *Rev1Xpc* mice and 7 age-matched *Xpc* littermates. **(F)** Expression of cellular senescence and aging-related genes $p16^{Ink4A}$ and *Gadd45a* in spleens from *Rev1Xpc* mice compared with spleens from age-matched *Xpc* littermates. **: $p<0.01$. **(G)** TUNEL staining for apoptotic bodies (red dots) in a *Rev1Xpc* spleen and an age-matched *Xpc* littermate. **(H)** Quantification of apoptotic bodies in spleens from *Rev1Xpc* and age-matched *Xpc* mice. ***: $p<0.001$. Error bars: SD.

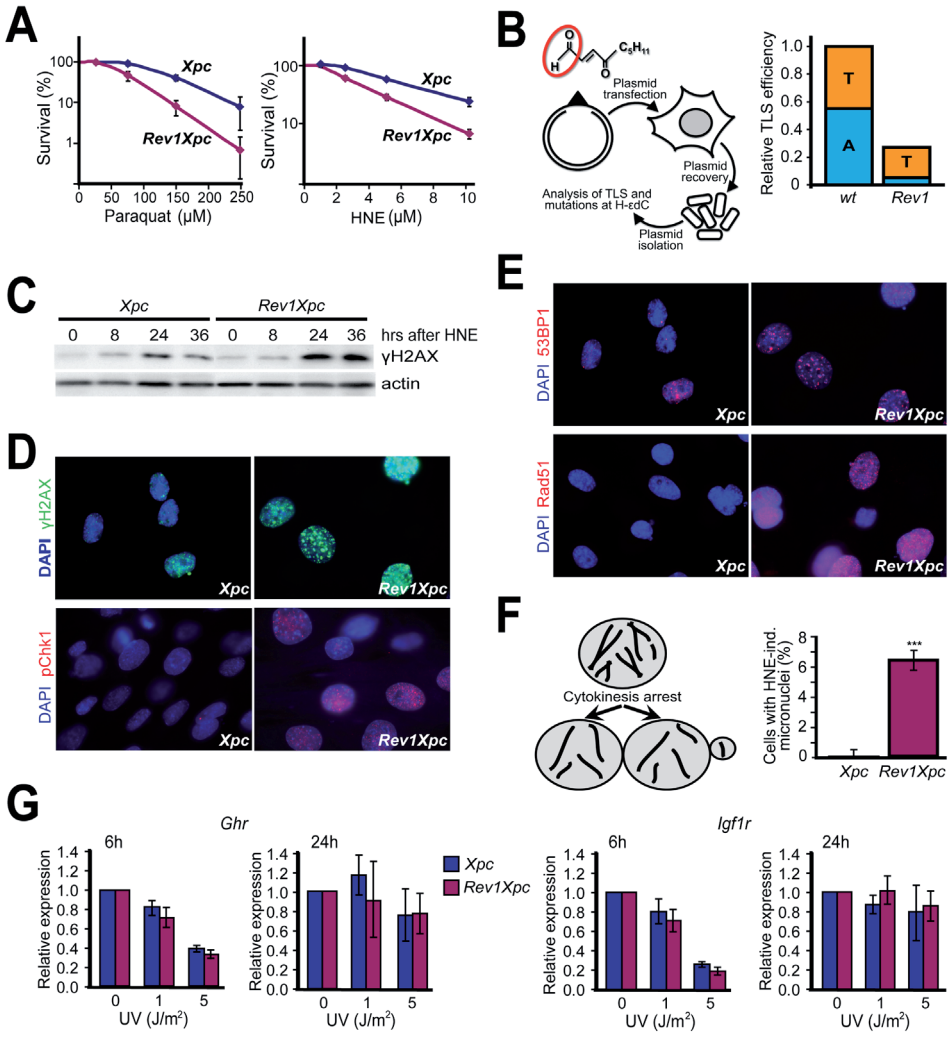

Figure 4 | DNA damage responses and genome instability in *Rev1* and *Rev1Xpc* MEFs. (A) Sensitivity of *Xpc* and *Rev1Xpc* MEFs to the oxidative stress-inducing agent Paraquat and the lipid peroxidation-derived hydroxyalkenal HNE. *n*=3, independent experiments. Error bars: SD. **(B)** Left panel: assay to measure the efficiency and mutagenicity of TLR at a site-specific H-εdC (structure at the top of the panel; the reactive aldehyde group is encircled). The opposing single-stranded DNA gap renders the lesion resistant to repair. Three days after transfection, covalently-closed plasmids are isolated from transfected MEFs and rescued in *E. coli*. Right panel: efficiency and mutagenicity of TLR at the H-εdC. T, A: incorporation of thymidine and adenine respectively. **(C)** Induction of γH2AX in *Xpc* and *Rev1Xpc* MEFs after exposure to 15μM HNE, analyzed by Western blotting. **(D)** Immunocytochemical analysis of the replicative stress markers γH2AX and pChk1 in *Xpc* and *Rev1Xpc* MEFs, 24h after exposure to 5μM HNE. **(E)** Induction of the double-strand DNA break markers 53BP1 and Rad51 in *Xpc* and *Rev1Xpc* MEFs, 24h after exposure to 5μM HNE. **(F)** Left panel: In the cytokinesis-block micronucleus assay cells are arrested during cytokinesis, which allows the quantification of chromatid fragment-containing micronuclei. Right panel: quantification of genome instability at 48h after exposure of *Xpc* and *Rev1Xpc* MEFs to equitoxic HNE doses, corrected for the dose used. *n*=3 independent experiments. ***: $p<0.001$. Error bars: SD. **(G)** mRNA levels in primary *Xpc* and *Rev1Xpc* MEFs of two key somatotrophic genes at 6 and 24h after exposure to different UV doses, as determined by quantitative PCR. *n*=3 independent experiments. Error bars: SD

In further support of a causal role of *Rev1* in suppressing replicative stress in response to hydroxalkenal-DNA adducts, exposure of *Rev1Xpc* MEFs to HNE induced phosphorylation of the stress markers Chk1 and of H2AX (Figs. 4C and D). Finally, HNE exposure of *Rev1Xpc*, but not *Xpc*, MEFs, induced foci of the double strand DNA breaks markers 53BP1 and Rad51 (Fig. 4E) and micronuclei that contain chromosomal fragments (Fig. 4F). These results indicate that in the absence of Rev1 replication forks collapse at hydroxalkenal-DNA adducts, resulting in genome instability. We hypothesize that genome instability originating from replicative stress at endogenous bulky DNA adducts sustains the development of lymphomas in *Rev1Xpc* mice.

Transcriptional stress induces a longevity-promoting response by suppressing the somato-, lacto- and thyrotrophic axes (Garinis *et al.*, 2009; Hoeijmakers, 2009; Niedernhofer *et al.*, 2006). We investigated whether also replicative stress induces this response. However, compared with *Xpc* MEFs (Garinis *et al.*, 2009), UV exposure of *Rev1Xpc* MEFs induced no exacerbated or prolonged suppression of the somatotropic genes *Ghr* and *Igf1r* (Fig. 4G). Furthermore, compared with age-matched *Xpc* mice, the level of the somatotrophic protein IGFBP1 was not altered in livers of progeroid *Rev1Xpc* mice (Fig. S9). Since, unlike replicative stress, transcriptional stress may occur in all aging cells, it may be a more appropriate inducer of the shift to maintenance in aging organisms.

We conclude that replicative stress at endogenous bulky DNA adducts induces the attrition of proliferating stem and differentiated cells that underlies the aging phenotypes of *Rev1* and, more pronounced, of *Rev1Xpc* mice (Fig. S1 for an integrative model). Each progeroid mouse model is believed to emphasize a segment of the pathology of physiological aging (Burtner *et al.*, 2010). The phenotypes of *Rev1* and *Rev1Xpc* mice, therefore, support a causal role for replicative stress also in physiological aging and associated carcinogenesis. Despite the fact that hydroxyalkenal-DNA adducts are substrates for GG-NER, these lesions accumulate to high levels during physiological aging, also in GG-NER-proficient mice and humans (Chou *et al.*, 2010; Wang *et al.*, 2012; Winczura *et al.*, 2012). Given their long lifespan it is not unlikely that replicative stress at bulky DNA adducts is a more prominent determinant of aging and associated cancer in humans than in mice.

MATERIALS AND METHODS

Mice and cell lines. *Rev1* and *Xpc* mice were described previously (Jansen *et al.*, 2006; Melis *et al.*, 2008). *Rev1* (*n*=32) and wild type (*n*=55) cohorts were of mixed 129OLA/SV and C57Bl/6 background. SKH (hairless, albino) *Xpc* and *Rev1Xpc* cohorts (*n*=17 each) were obtained from backcrossing $Rev1^{+/-}Xpc^{-/-}$ parents. MEF lines were obtained from 13.5-day embryos by spontaneous immortalization. Survival was measured by clonogenic or proliferation assays.

Histology. Mouse tissues were fixed in Bouin or Harrison's fixative, and paraffin-embedded sections were stained by Haematoxylin and/or Eosin (HE). Pathological examination was performed on coded samples. Karyomegaly and lipofuscin deposits were quantified by grading

4 coded sections per mouse from 0-3, using 8 mice per genotype. Epidermal cell layers were counted on 4 coded sections per mouse, using 8 mice per genotype. Two-tailed T tests were used to calculate significance.

Analysis of the hematopoietic system. Isolation of hematopoietic precursor populations and HSCs and competitive transplantation experiments using HSCs were performed as described (Dykstra *et al.*, 2011). CAFC assays were performed on stromal cells, as described (van Os *et al.*, 2008). Colony sizes were determined using cytokine-supplemented media, as described (Dykstra *et al.*, 2011).

Flow cytometry analysis, immunohistochemistry and Western blotting. Splenocytes were isolated from 6-7 mice per genotype. T cell subsets were stained using anti-CD4 and anti-CD8 antibodies and immature B cells were stained using anti-IgM and anti-IgD antibodies, as described (Jansen *et al.*, 2006). Immunohistochemistry and Western blotting were performed using established protocols. Apoptosis was assessed by TUNEL staining and quantified on 2 coded Cytospin-precipitated splenocyte samples per mouse, using 4 mice per genotype. Significance was assessed by two-tailed T test.

TLR assay. The generation of a site-specific single-stranded H-εdC lesion and the determination of the efficiency and mutagenicity of TLR was performed essentially as described for a benzo[*a*] pyrene-dG adduct (Hashimoto *et al.*, 2012) (Fig. 4B).

Cytokinesis-block micronucleus assay. *Xpc* and *Rev1Xpc* MEFs were treated with equitoxic doses of HNE (9 μM and 5 μM, respectively). Chromatid breaks were quantified in cells blocked at cytokinesis (Fenech, 1993) (Fig. 4F). Results were analysed using a two-tailed T-test.

Quantitative PCR. Somatotrophic gene expression in UV-treated MEFs and senescence-related gene expression in mice were measured as described (Garinis *et al.*, 2009).

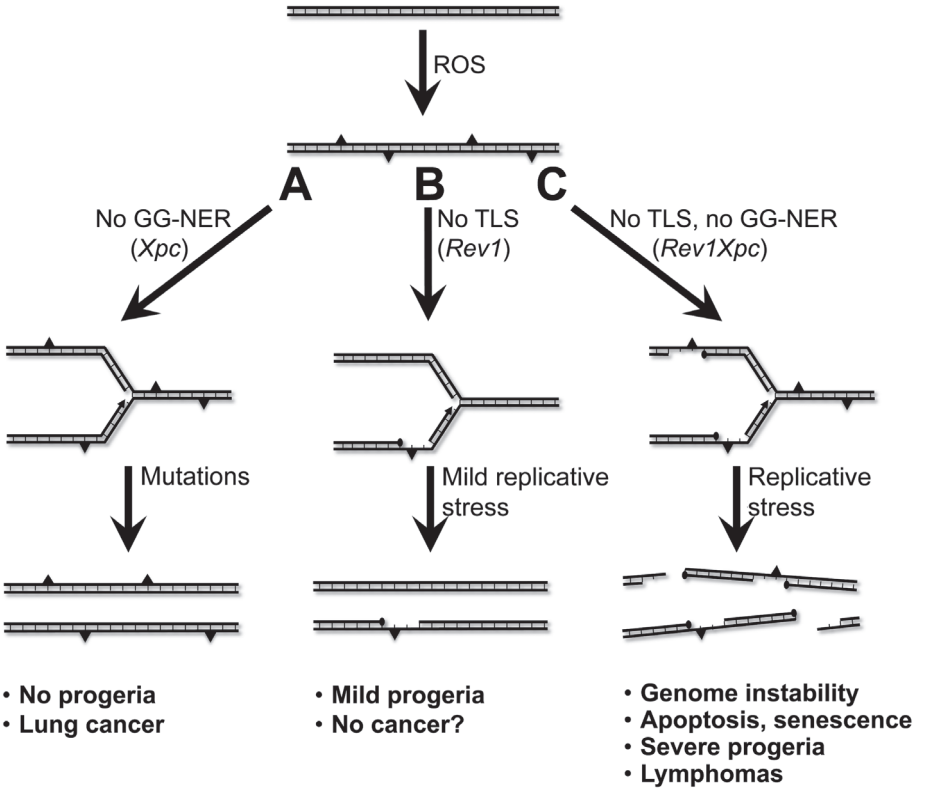

Figure S1 | GG-NER and TLR deficiencies differentially affect cancer predisposition and aging. Top: genomic DNA is damaged continuously by endogenous sources, including ROS that, in addition to base damages, induces bulky nucleotide lesions (triangles). **(A)** Deficiency of GG-NER of endogenous bulky nucleotide lesions leads to a TLR-dependent accumulation of mutations that may underlie the predisposition to spontaneous lung tumors in old *Xpc* mice (Melis *et al.,* 2008). **(B)** Deficiency of TLR results in mild replicative stress at endogenous bulky nucleotide lesions that have escaped GG-NER. This is associated with mild progeroid features, but not with obvious cancer predisposition. **(C)** Combined TLR and GG-NER deficiency leads to severe replicative stress at endogenous bulky nucleotide lesions. This induces genome instability, apoptosis and senescence in proliferating compartments and, consequently, accelerated aging. The genomic instability, combined with escape from apoptosis and senescence, may underlie the development of aging-associated lymphomas.

A

Rev1$^{+/-}$ X *Rev1*$^{+/-}$	Number of progeny genotyped	*Rev1* progeny		
		observed	expected	observed/ expected
13.5-day embryos	74	17 (22%)	19 (25%)	0.9 (p=0.78)
10-day pups	436	67 (15.5%)	109 (25%)	0.6 (p<0.001)

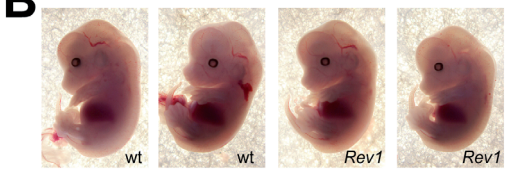

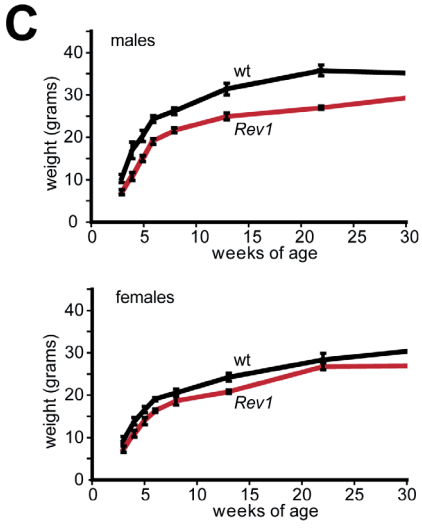

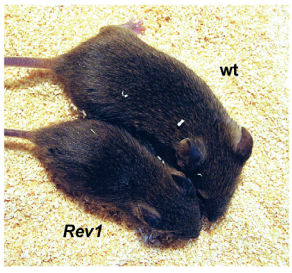

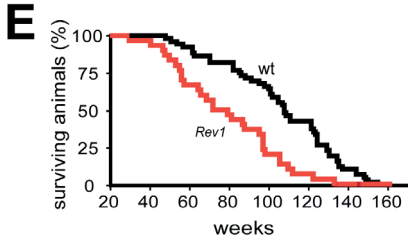

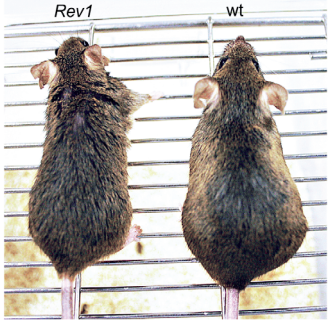

Figure S2 | Phenotypes of *Rev1* embryos and mice. **(A)** Frequency of 13.5-day *Rev1* embryos and pups from *Rev1*$^{+/-}$ backcrosses. **(B)** *Rev1* embryos at day 13.5 of gestation are undistinguishable from wild type controls. **(C)** Body weights of *Rev1* male and female mice and wild type littermates. Data derived from (Jansen *et al.*, 2006). **(D)** *Rev1* mice of 2 months of age display a variably reduced body size but no other overt phenotypes. Reproduced from (Jansen *et al.*, 2006). **(E)** Reduced lifespan of *Rev1* mice (*Rev1*: n=32, t_{50}=75 weeks; wild type: n=55, t_{50}=108 weeks; p<0.05, Mann-Whitney test). **(F)** An 18-month old *Rev1* mouse displaying ruffling of the fur.

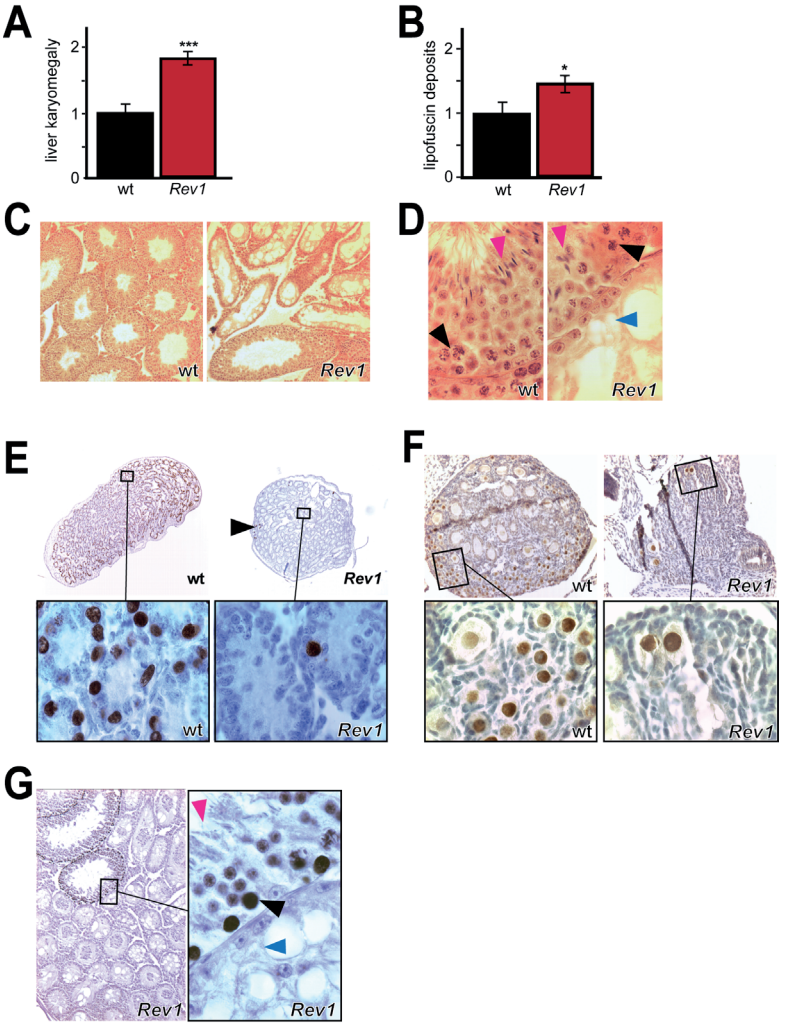

Figure S3 | Phenotypes of *Rev1* liver and gonads. (A) Quantification of hepatic karyomegaly in (18-months old) *Rev1* and age-matched *Xpc* mice. *n*= 8 mice, ***: $p<0.001$. Error bars: SD. **(B)** Quantification of hepatic lipofuscin in (18-months old) *Rev1* mice and age-matched *Xpc controls*. *n*=8 mice, *: $p=0.011$. Error bars: SD. See the legend to Fig. 2C for experimental details. Bouin-fixed sections reveal a lack of spermatogenic stages in most seminiferous tubules in testis from a 2-month old *Rev1* mouse. **(C-D)** Residual spermatogenesis (arrowhead) in a testis of a 2-month old *wt* and *Rev1* mouse. Black arrowhead: meiotic (anaphase) cells, Purple arrowhead: early spermatids. Blue arrowhead: the lower tubule is devoid of spermatogenic stages. **(E)** Staining for GCNA1 (brown) in testes from a 6 day-old *wt* and *Rev1*. Loss of GCNA1 staining in *Rev1* male demonstrates the early attrition of germ stem cells. Sections were counterstained with hematoxylin and were the same as depicted in Figure 1B. Arrowhead: GCNA1-positive tubules. Bottom panels: magnified sections displaying rare GCNA1-positive germ cells in the *Rev1* male. **(F)** Staining for GCNA1 (brown) in ovaries from a 6 day-old *wt* and *Rev1*. Loss of GCNA1 staining in *Rev1* female demonstrates the early attrition of germ stem cells. Sections were counterstained with hematoxylin. Bottom panels: magnified sections displaying residual GCNA1-positive germ cells in the *Rev1* female. **(G)** GCNA1 staining (brown) confirms the presence of a low fraction of normal testicular tubules of an adult *Rev1* mouse. Sections were counterstained with hematoxylin. Right panel: magnification displaying GCNA1-positive germ cells (black arrowhead) and early spermatids (purple arrowhead).

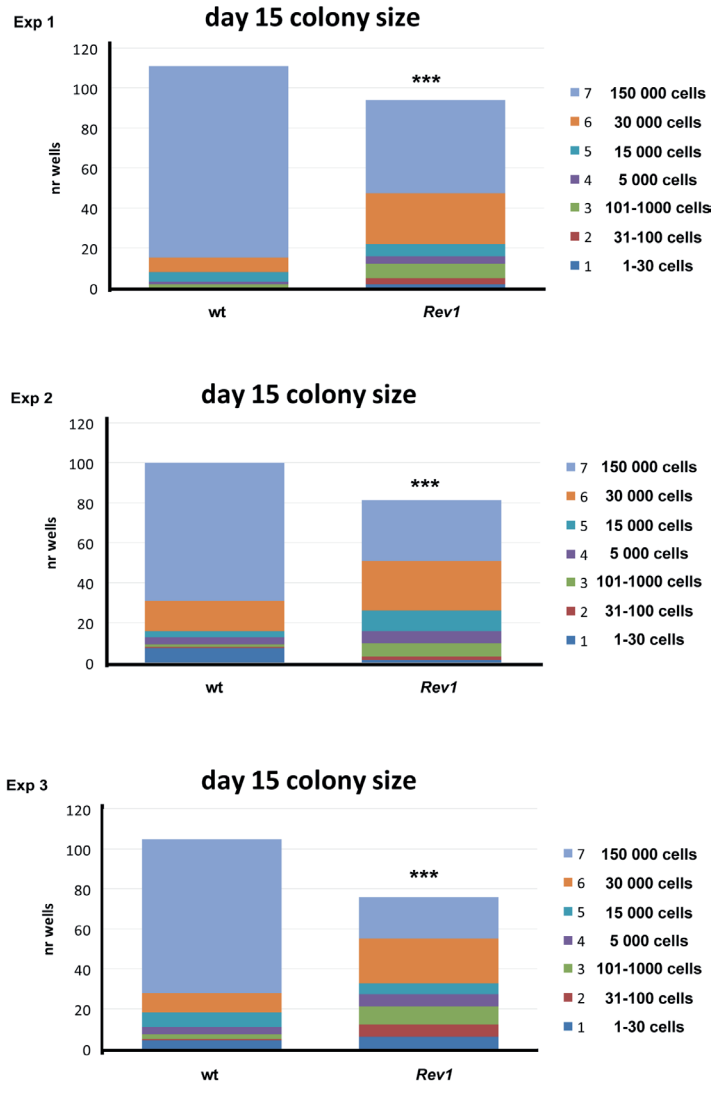

Figure S4 | Reduced sizes of *Rev1* HSC clones. HSCs from three 18-month-old *Rev1* and three wild type mice were seeded in cytokine-supplemented medium and colony sizes were determined at 15 days after seeding. X^2 test, ***: $p<0.001$. Error bars: SD.

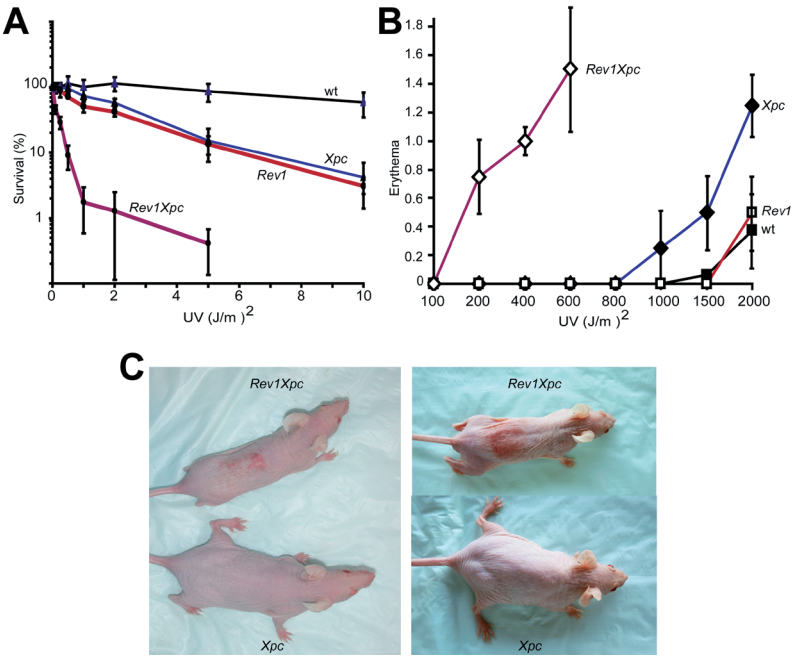

Figure S5 | Sensitivity of *Xpc*, *Rev1* and *Rev1Xpc*-deficient cells and mice to UV-induced photolesions. **(A)** Clonal survival of UVC-exposed wild type, *Rev1*, *Xpc* and *Rev1Xpc* MEFs. *n*=4 independent experiments. Error bars: SD. **(B)** Sensitivity of skin of hairless albino wild type, *Rev1*, *Xpc* and *Rev1Xpc* mice, 7 days after local exposure to artificial sunlight. *n*=4 per dose per genotype. Error bars: SD. **(C)** Induction of erythema in 2-months old *Rev1Xpc* mice, but not in age-matched *Xpc* controls, locally exposed to 40 J/m^2 of artificial sunlight per day, during 5 subsequent days.

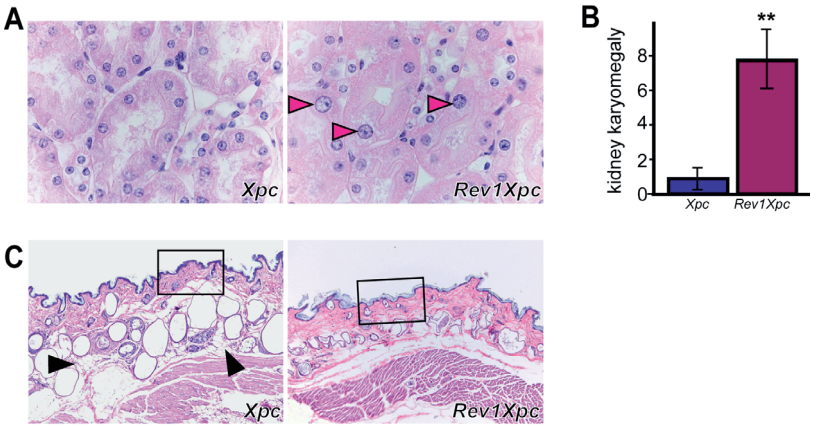

Figure S6 | Degenerative phenotypes in organs of progeroid *Rev1Xpc* mice. **(A)** HE staining of a kidney section from a *Rev1Xpc* mouse and an age-matched *Xpc* control. Purple arrowheads: karyomegaly. **(B)** Relative levels of renal karyomegaly in *Rev1Xpc* mice, compared with age-matched *Xpc* controls. *n*= 8 mice, **: $p<0.01$. Error bars: SD. **(C)** HE staining of skin sections. Black arrowheads: subdermal fat in the *Xpc* mouse. Black rectangles: sections magnified in Fig. 2I.

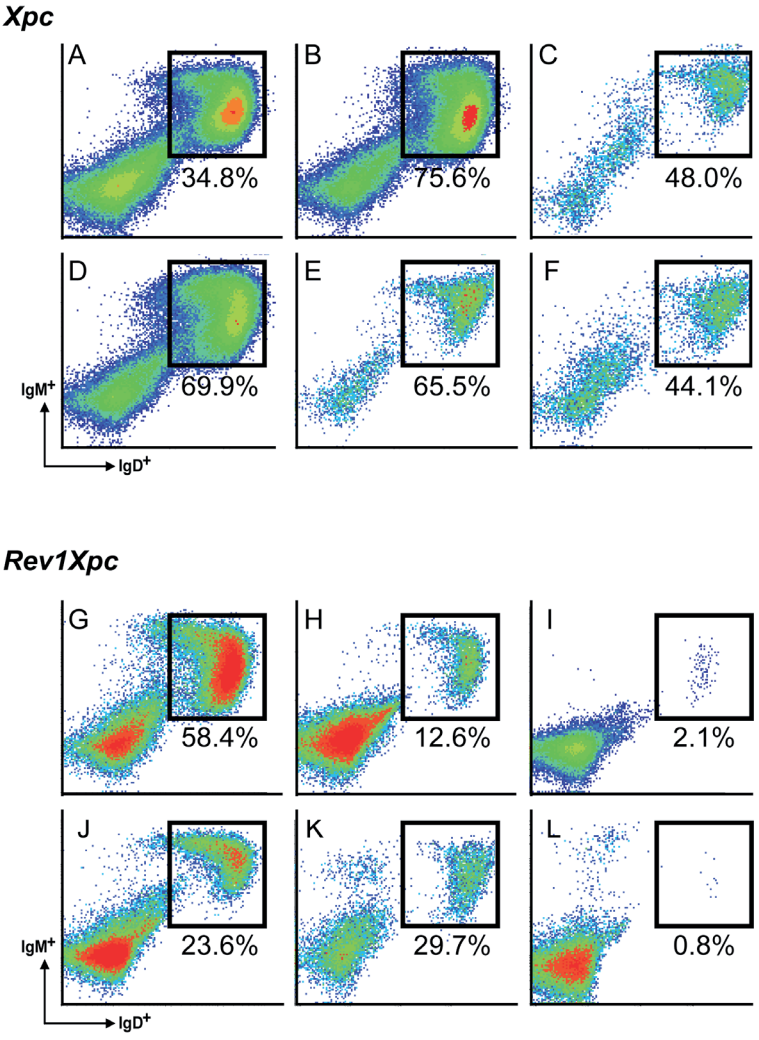

Figure S7 | Analysis of B lymphocytes in spleens of progeroid *Rev1Xpc* mice and age-matched *Xpc* controls. (A-F) Fluorescence cytometry analysis and quantification (% of total cell counts) of IgD^+IgM^+ B cells in spleens of 6 adult *Xpc* mice. Panel B represents the same mouse as Fig. 3A (left). **(G)** Fluorescence cytometry analysis and quantification (% of total cell counts) of IgD^+IgM^+ B cells in the spleen of a young *Rev1Xpc* mouse demonstrating that the B cell compartment is normal at young age. **(H-L)** Fluorescence cytometry analysis and quantification (% of total cell counts) of IgD^+IgM^+ B cells in 5 spleens of progeroid *Rev1Xpc* mice (age-matched with the *Xpc* controls analyzed in panels A-F). Panel H represents the same mouse as Fig. 3A (right panel).

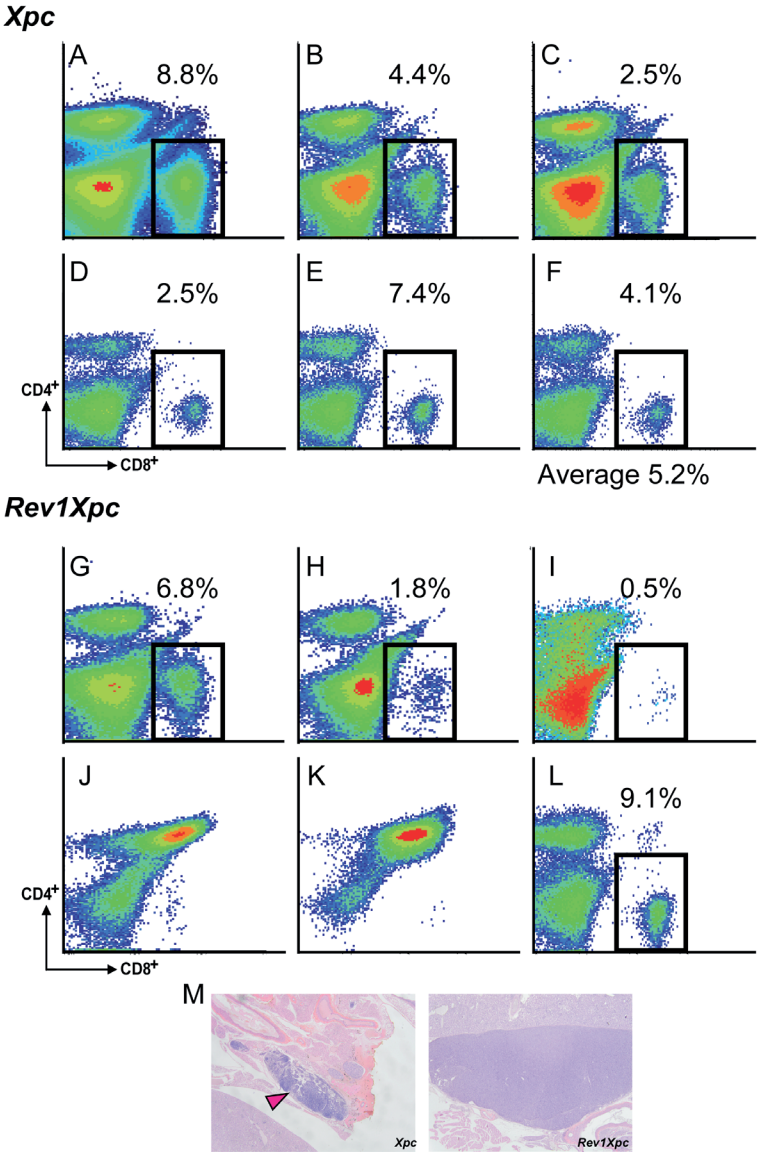

Figure S8 | Analysis of T lymphocytes in spleens of *Rev1Xpc* mice. Mice were the same as in Fig. S7. **(A-F)** Fluorescence cytometry analysis and quantification (% of total cell counts) of $CD4^+$ and $CD8^+$ T cells in spleens of 6 adult *Xpc* mice. Panel B represents the same mouse as Fig. 3C. Fluorescence cytometry analysis and quantification (% of total cell counts) of $CD4^+$ and $CD8^+$ T cells in the spleen of a young *Rev1Xpc* mouse demonstrating that the T cell compartment is normal at young age. **(H-I)** Fluorescence cytometry analysis and quantification (% of total cell counts) of $CD4^+$ and $CD8^+$ T cells in spleens of progeroid *Rev1Xpc* mice reveal a reduction in the numbers of $CD8^+$ T cells. Panel H represents the same mouse as Fig. 3C (right panel). **(J-K)** $CD4^+CD8^+$ T cell lymphomas in two progeroid *Rev1Xpc* mice. Panel K represents the same mouse as Fig. 3D. **(L)** Increased level of CD8 expression (rightward shift) of $CD8^+$-positive T cells in a progeroid *Rev1Xpc* mouse. **(M)** $CD4^+CD8^+$ T cell lymphoma in a mesenterial lymph node in a progeroid *Rev1Xpc* mouse. Purple arrowhead: normal mesenterial lymph node.

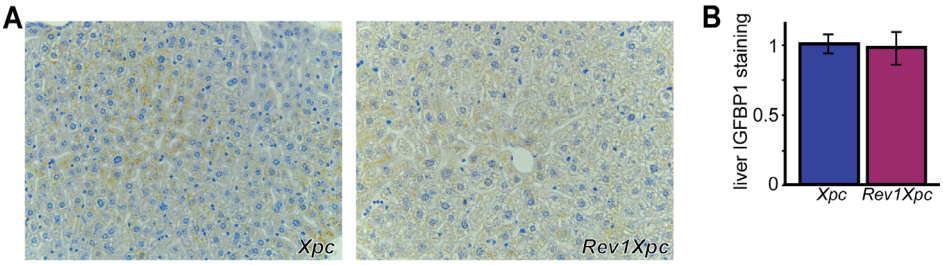

Figure S9 | Expression of the somatotrophic protein IGF1R in liver. A. Expression of IGFBP1 (brown) in livers of a progeroid *Rev1Xpc* and an age-matched *Xpc* mouse. B. Relative levels of IGFBP1 expression in liver of progeroid *Rev1Xpc* mice, compared with age-matched *Xpc* controls. No differential IGFBP1 expression is observed. *n*=8 mice each. Error bars: SD.

Table S1 | Pathological examination of the mouse cohorts

Mouse #, genotype, age (months)[1], sex	Liver	Bone marrow	Skin	Other pathologies
007, wt, 28, ♀				Chronic inflammation. Possible B-cell hyperplasia.
008, wt, 28, ♂	Reactive hepatitis. Possible hepatoma.		Mild atrophy of hair follicles and sebaceous glands	Thyroid carcinoma. Possible lymphoma.
010, wt, 25, ♀				Lymphoid hyperplasia.
012, wt, 24, ♂				Early stage B-cell lymphoma.
013, wt, 24, ♂				B-cell hyperplasia.
016, wt, 22, ♀	Hemangioma.			B-cell lymphoma.
018, wt, 19, ♀				Chronic inflammation. Possible B-cell hyperplasia.
185, *Rev1*, 19, ♀	Fatty vacuolisation. Cytoplasmic glycogenosis. Steatosis. Lipofuscin accumulation. Karyomegaly.	Hypoplasia.		Kidney: chronic inflammation. Hyalin deposits (Hill *et al.*, 2003) in glomerular membranes. Lymphoid follicular atrophy
186, *Rev1*, 19, ♀	Fatty vacuolisation. Cytoplasmic glycogenosis. Steatosis. Lipofuscin accumulation. Karyomegaly.	Hypoplasia.	Atrophy of hair follicles and sebaceous glands	B-cell lymphoma. Osteosclerosis. Lymphoid follicular atrophy
187, *Rev1*, 21, ♂	Fatty vacuolisation. Cytoplasmic glycogenosis. Lipofuscin accumulation. Karyomegaly.	Hypoplasia.		Kidney: Hyalin deposits in glomerular membranes.
005, Rev1, 28, ♀	Steatosis.	Hypoplasia.		B-cell lymphoma. Lymphoid follicular atrophy.
006, Rev1, 28, ♀	Lipofuscin accumulation.		Atrophy of hair follicles and sebaceous glands.	B-cell lymphoma. Hemangioma in ovary.
009, Rev1, 25, ♀		Hypoplasia.	Mild atrophy of hair follicles and sebaceous glands.	Mild tubular degeneration in liver.
011, Rev1, 24, ♂	Steatosis.	Hypoplasia.	Atrophy of hair follicles and sebaceous glands.	Lymphoma
014, Rev1, 24, ♂	Steatosis.		Mild atrophy of hair follicles and sebaceous glands.	Papillary adenoma in uterus.
049, Rev1, 25, ♂	Karyomegaly.	Hypoplasia.	Atrophy of hair follicles and sebaceous glands.	

Table S1 | Pathological examination of the mouse cohorts (*continued*)

Mouse #, genotype, age (months)[1], sex	Liver	Bone marrow	Skin	Other pathologies
005, Rev1, 28, ♀	Steatosis.			
006, Rev1, 28, ♀	Lipofuscin accumulation. Karyomegaly.	Hypoplasia.	Atrophy of hair follicles and sebaceous glands.	
002, Xpc, 8, ♀				
003, Xpc, 6, ♀				
004, Xpc, 10, ♀				
043, Xpc, 8, ♀				
046, Xpc, 13, ♂				
047, Xpc, 12, ♀				
048, Xpc, 10, ♀				
052, Xpc, 8, ♀		Aplastic anaemia.	Atrophic epidermis. Lack of subcutaneous fat.	Kidney: karyomegaly.
180, Rev1Xpc, 7, ♀	Mild glycogenosis. Lipofuscin accumulation. Karyomegaly.	Aplastic anaemia.	Atrophic epidermis. Lack of subcutaneous fat	Kidney: karyomegaly, tubular degeneration.
181, Rev1Xpc, 10, ♀	Mild glycogenosis. Lipofuscin accumulation. Karyomegaly.	Aplastic anaemia.	Atrophic epidermis. Lack of subcutaneous fat	Kidney: karyomegaly, tubular degeneration.
182, Rev1Xpc, 13, ♀	Karyomegaly.	Aplastic anaemia.		Kidney: severe karyomegaly.
042, Rev1Xpc, 8, ♂	Steatosis.	Aplastic anaemia.	Atrophic epidermis. Lack of subcutaneous fat	Kidney: severe anisokaryosis, tubular degeneration.
044, Rev1Xpc, 11, ♀	Karyomegaly.			Kidney: tubular degeneration.
045, Rev1Xpc, 13, ♂ (not moribund)	Steatosis.	Aplastic anaemia.	Atrophic epidermis. Lack of subcutaneous fat	Possible lymphoma.
050, Rev1Xpc, 6, ♀	Karyomegaly.	Hypoplasia.	Atrophic epidermis. Lack of subcutaneous fat	Osteoporosis.
051, Rev1Xpc, 7, ♀	Karyomegaly.	Aplastic anaemia.	Atrophic epidermis. Lack of subcutaneous fat	Lymphoma.
053, Rev1Xpc, 6, ♀	Karyomegaly.	Aplastic anaemia.	Atrophic epidermis. Lack of subcutaneous fat.	Osteoporosis.

[1] *Rev1Xpc* and *Rev1* mice were euthanized and autopsied when moribund. The age-matched *Xpc* and wild type littermates were sacrificed before the onset of end-of-life pathology.

REFERENCES

Burtner CR, Kennedy BK (2010). Progeria syndromes and aging: what is the connection? *Nat Rev Mol Cell Biol*. **11:** *567-578*

Chen L, Hu JY, Wang SQ (2012). The role of antioxidants in photoprotection: a critical review. *J Am Acad Dermatol*. **67:** *1013-1024*

Chou PH, Kageyama S, Matsuda S, Kanemoto K, Sasada Y, Oka M, Shinmura K, Mori H, Kawai K, Kasai H *et al.* (2010). Detection of lipid peroxidation-induced DNA adducts caused by 4-oxo-2(E)-nonenal and 4-oxo-2(E)-hexenal in human autopsy tissues. *Chem Res Toxicol*. **23:** *1442-1448*

Dykstra B, Olthof S, Schreuder J, Ritsema M, de Haan G (2011). Clonal analysis reveals multiple functional defects of aged murine hematopoietic stem cells. *J Exp Med*. **208:** *2691-2703*

Fenech M (1993). The cytokinesis-block micronucleus technique: a detailed description of the method and its application to genotoxicity studies in human populations. *Mutat Res*. **285:** *35-44*

Frith CH, Wiley LD (1981). Morphologic classification and correlation of incidence of hyperplastic and neoplastic hematopoietic lesions in mice with age. *J Gerontol*. **36:** *534-545*

Garinis GA, Uittenboogaard LM, Stachelscheid H, Fousteri M, van Ijcken W, Breit TM, van Steeg H, Mullenders LH, van der Horst GT, Bruning JC *et al.* (2009). Persistent transcription-blocking DNA lesions trigger somatic growth attenuation associated with longevity. *Nat Cell Biol*. **11:** *604-615*

Geiger H, Rudolph KL (2009). Aging in the lympho-hematopoietic stem cell compartment. *Trends Immunol*. **30:** *360-365*

Gorla GR, Malhi H, Gupta S (2001). Polyploidy associated with oxidative injury attenuates proliferative potential of cells. *J Cell Sci*. **114:** *2943-2951*

Hashimoto K, Cho Y, Yang IY, Akagi J, Ohashi E, Tateishi S, de Wind N, Hanaoka F, Ohmori H, Moriya M (2012). The vital role of polymerase zeta and REV1 in mutagenic, but not correct, DNA synthesis across benzo[a]pyrene-dG and recruitment of polymerase zeta by REV1 to replication-stalled site. *J Biol Chem*. **287:** *9613-9622*

Hill GS, Heudes D, Bariety J (2003). Morphometric study of arterioles and glomeruli in the aging kidney suggests focal loss of autoregulation. *Kidney Int*. **63:** *1027-1036*

Hoeijmakers JH (2009). DNA damage, aging, and cancer. *N Engl J Med*. **361:** *1475-1485*

Jansen JG, Langerak P, Tsaalbi-Shtylik A, van den Berk P, Jacobs H, de Wind N (2006). Strand-biased defect in C/G transversions in hypermutating immunoglobulin genes in Rev1-deficient mice. *J Exp Med*. **203:** *319-323*

Langevin F, Crossan GP, Rosado IV, Arends MJ, Patel KJ (2011). Fancd2 counteracts the toxic effects of naturally produced aldehydes in mice. *Nature*. **475:** *53-58*

Maslov AY, Vijg J (2009). Genome instability, cancer and aging. *Biochim Biophys Acta*. **1790:** *963-969*

Melis JP, Wijnhoven SW, Beems RB, Roodbergen M, van den Berg J, Moon H, Friedberg E, van der Horst GT, Hoeijmakers JH, Vijg J *et al.* (2008). Mouse models for xeroderma pigmentosum group A and group C show divergent cancer phenotypes. *Cancer Res*. **68:** *1347-1353*

Niedernhofer LJ, Garinis GA, Raams A, Lalai AS, Robinson AR, Appeldoorn E, Odijk H, Oostendorp R, Ahmad A, van Leeuwen W *et al.* (2006). A new progeroid syndrome reveals that genotoxic stress suppresses the somatotroph axis. *Nature*. **444:** *1038-1043*

Passos JF, Nelson G, Wang C, Richter T, Simillion C, Proctor CJ, Miwa S, Olijslagers S, Hallinan J, Wipat A *et al.* (2010). Feedback between p21 and reactive oxygen production is necessary for cell senescence. *Mol Syst Biol*. **6:** *347*

Rossi DJ, Bryder D, Seita J, Nussenzweig A, Hoeijmakers J, Weissman IL (2007). Deficiencies in DNA damage repair limit the function of haematopoietic stem cells with age. *Nature*. **447:** *725-729*

Ruzankina Y, Asare A, Brown EJ (2008). Replicative stress, stem cells and aging. *Mech Aging Dev*. **129:** *460-466*

Sale JE, Lehmann AR, Woodgate R (2012). Y-family DNA polymerases and their role in tolerance of cellular DNA damage. *Nat Rev Mol Cell Biol*. **13:** *141-152*

Storms RW, Green PD, Safford KM, Niedzwiecki D, Cogle CR, Colvin OM, Chao NJ, Rice HE, Smith CA (2005). Distinct hematopoietic progenitor compartments are delineated by the expression of aldehyde dehydrogenase and CD34. *Blood*. **106:** *95-102*

Thoolen B, Maronpot RR, Harada T, Nyska A, Rousseaux C, Nolte T, Malarkey DE, Kaufmann W, Kuttler K, Deschl U *et al.* (2010). Proliferative and nonproliferative lesions of the rat and mouse hepatobiliary system. *Toxicol Pathol*. **38:** *5S-81S*

Turner TT, Lysiak JJ (2008). Oxidative stress: a common factor in testicular dysfunction. *J Androl*. **29:** *488-498*

van Os RP, Dethmers-Ausema B, de Haan G (2008). In vitro assays for cobblestone area-forming cells, LTC-IC, and CFU-C. *Methods Mol Biol*. **430:** *143-157*

Wang C, Jurk D, Maddick M, Nelson G, Martin-Ruiz C, von Zglinicki T (2009). DNA damage response and cellular senescence in tissues of aging mice. *Aging Cell*. **8:** *311-323*

Wang D, Enders GC (1996). Expression of a specific mouse germ cell nuclear antigen (GCNA1) by early embryonic testicular teratoma cells in 129/Sv-Sl/+ mice. *Cancer Lett*. **100:** *31-36*

Wang J, Clauson CL, Robbins PD, Niedernhofer LJ, Wang Y (2012). The oxidative DNA lesions 8,5'-cyclopurines accumulate with aging in a tissue-specific manner. *Aging Cell*. **11:** *714-716*

Winczura A, Zdzalik D, Tudek B (2012). Damage of DNA and proteins by major lipid peroxidation products in genome stability. *Free Radic Res*. **46:** *442-459*

Yahata T, Takanashi T, Muguruma Y, Ibrahim AA, Matsuzawa H, Uno T, Sheng Y, Onizuka M, Ito M, Kato S *et al.* (2011). Accumulation of oxidative DNA damage restricts the self-renewal capacity of human hematopoietic stem cells. *Blood*. **118:** *2941-2950*